electronics

MDPI

Article

Reconstruction of Impedance Criteria and Stability Enhancement Strategies for Grid-Connected Inverters

Haoyu Mao and Xiaohui Yang *

School of Information Engineering, Nanchang University, Nanchang 330031, China; 5811123074@email.ncu.edu.cn
* Correspondence: yangxiaohui@ncu.edu.cn

Abstract

Grid-connected inverters play an indispensable and crucial role between new energy power generation devices and the power grid. As an important method for stability analysis of grid-connected inverters, impedance criteria have been widely applied. However, traditional impedance criteria have the problem of inaccurately representing system stability margins. Moreover, under weak grid conditions where grid impedance cannot be ignored, voltage disturbances at the point of common coupling will cause phase angle deviations in the output of the phase-locked loop, thereby affecting the stability of the control system. To address these issues, this paper establishes a stability analysis model based on the reshaping of impedance criteria and proposes a q-axis improved control compensation method, which expands the adaptability range of grid impedance for inverters and enhances the stability of grid-connected inverters. Finally, the correctness of the proposed algorithm is verified through experiments.

Keywords: phase-locked loops; grid-tied inverter; impedance criterion remodeling; stability analysis; small-signal compensation

check for updates

Academic Editor: Fabio Corti

Received: 9 October 2025
Revised: 6 November 2025
Accepted: 10 November 2025
Published: 12 November 2025

Citation: Mao, H.; Yang, X. Reconstruction of Impedance Criteria and Stability Enhancement Strategies for Grid-Connected Inverters. *Electronics* **2025**, *14*, 4402. https://doi.org/10.3390/electronics14224402

Copyright: © 2025 by the authors. Licensee MDPI, Basel, Switzerland. This article is an open access article distributed under the terms and conditions of the Creative Commons Attribution (CC BY) license (https://creativecommons.org/licenses/by/4.0/).

1. Introduction

Due to their environmentally friendly and renewable nature, new energy sources have become increasingly important in today's society facing energy shortages, thereby promoting the continuous advancement of new energy generation technologies [1,2]. As a bridge between renewable energy generation units and the power grid, grid-connected inverters are responsible for injecting the generated electrical energy into the grid in a stable and high-quality manner [3,4]. However, certain renewable generation units are connected at the end of the grid, where long transmission lines make the line impedance non-negligible. In contrast, off-grid residential photovoltaic systems, which lack long-distance transmission lines, have very small or even negligible line impedance. Therefore, grid-connected inverters for renewable energy operate under conditions with significant variations in line impedance, and the impedance characteristics can significantly impact their stable operation [5,6]. Consequently, stability analysis of renewable energy grid-connected inverters under a wide range of line impedance conditions has significant practical engineering value.

References [7,8] analyze the stability of the control system by establishing the state-space matrix of the grid-connected inverter and plotting the eigenvalues of the state transition matrix. However, when analyzing complex current controllers or multi-inverter parallel systems, the dimension of the state-space matrix becomes very large, leading to

difficulties in modeling and increased analytical complexity. References [9,10] investigate the stability of the control system by developing an output impedance model of the grid-connected inverter and applying the impedance-based criterion. Nevertheless, the traditional impedance criterion suffers from inaccuracy in determining the stability margin. Reference [11] points out that the stability of grid-connected inverters is determined by two aspects: the initial parameters of the system control loop and the interaction between the inverter output impedance and the grid impedance. Therefore, the system stability margin must comprehensively account for both factors and cannot be replaced solely by the impedance interaction in the conventional impedance criterion. However, the study does not consider the impact of phase angle deviations in the phase-locked loop (PLL) on the inverter output impedance.

Reference [12] reduces the impact of phase angle deviations from the phase-locked loop (PLL) on the inverter output impedance by lowering the PLL bandwidth; however, this approach deteriorates the dynamic performance of the control system. To address this issue, References [13,14] modify the PLL structure, enabling the system to maintain strong immunity against grid impedance disturbances even under high bandwidth. Nevertheless, the PLL configuration becomes overly complex, making modeling and stability analysis difficult. Without altering the PLL structure or bandwidth, References [15,16] enhance the magnitude and phase of the inverter output impedance by introducing virtual impedance into the current control loop, thereby preventing instability caused by an insufficient phase margin at the crossover frequency. However, this method increases the regulation time of the control system. References [17,18] develop an inverter output impedance model that accounts for PLL phase angle deviations and analyzes both the extent and mechanism of their impact on the control system. Building on this, Reference [19] introduces a PLL phase-angle disturbance compensation term into the control loop to counteract the adverse effects of PLL phase deviations. This method improves the magnitude and phase margin of the inverter output impedance in the low- and mid-frequency range; nevertheless, as the frequency increases, its ability to enhance the phase margin at the crossover frequency diminishes, leaving the risk of instability under wide variations in grid impedance.

To enhance the adaptability of grid-connected inverters under wide variations in grid impedance and to accurately reflect the actual phase margin of the system, this paper first proposes a stability analysis method based on reshaped impedance criteria. This method can precisely characterize the true stability margin of the system and provides a theoretical foundation for evaluating the stability of grid-connected inverters under different grid conditions. On this basis, a novel compensation control method is further proposed by introducing a PLL disturbance compensation term into the control system. This method effectively improves the phase margin at the high-frequency crossover point and enhances the inverter's adaptability to wide-range grid impedance.

2. VSG Control Principle and Performance Analysis

Figure 1 shows the main circuit model of the grid-connected inverter and its control block diagram, where U_{dc} is the DC voltage; C_{dc1} and C_{dc2} are the DC-link capacitors; L_{f1}, L_{f2} and C_f are the inductors and capacitor of the LCL filter; L_g is the grid-side inductor; e_a, e_b and e_c are the grid voltages; u_{ao}, u_{bo} and u_{co} are the bridge arm output voltages; i_{ca}, i_{cb} and i_{cc} are the filter capacitor currents, expressed in the $\alpha\beta$-axis as $i_{c\alpha}$ and $i_{c\beta}$; u_{ga}, u_{gb} and u_{gc} are the inverter output voltages; i_{ga}, i_{gb} and i_{gc} are the inverter output currents, expressed in the dq-axis as i_{gd} and i_{gq}; θ_{pll} is the output angle of the PLL; i_{gdref} and i_{gqref} are the dq-axis current reference values; K_f is the decoupling term and equals $\omega_n(L_{f1}+L_{f2})$ where ω_n is the rated angular frequency of the grid; K_d is the active damping coefficient; and k_p and k_i are the proportional and integral coefficients of the PI controller, respectively.

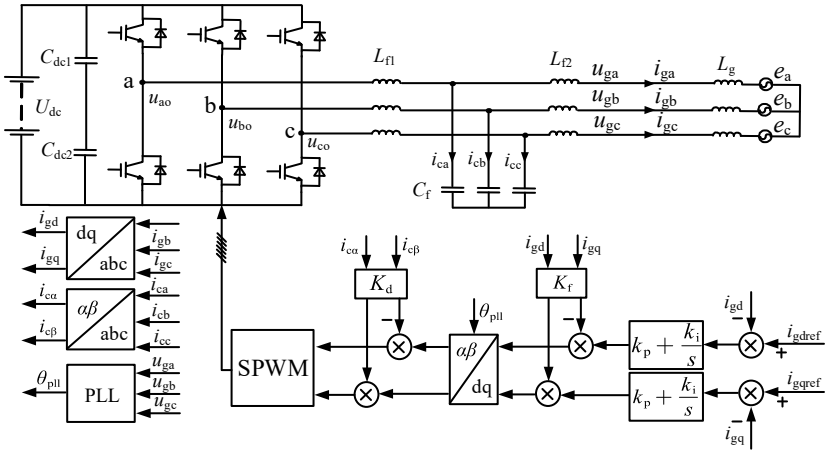

Figure 1. Inverter main circuit model and control system.

Under weak grid conditions, dynamic disturbances between the grid impedance and the inverter cause a phase difference $\Delta\theta$ between the actual phase angle of the grid voltage and the output angle of the PLL. According to the conclusion of Reference [20], the dq-axis closed-loop small-signal equivalent model of the grid-connected inverter under the influence of $\Delta\theta$ is as shown in Figure 2. In the figure, K_d is the active damping coefficient; u_{gd} and u_{gq} are the small-signal expressions of the PCC voltage in the dq-axis; i_{gd} and i_{gq} are the small-signal expressions of the PCC current in the dq-axis; i_{gd_ref} and i_{gq_ref} are the small-signal expressions of the PCC current references in the dq-axis; $T_{pll}(s)$ is the transfer function of the PLL; U_{gd} and I_{gd} are the rated values of the PCC voltage and current on the d-axis; $G_d(s)$ is the delay function; $G_1(s)$ and $G_2(s)$ are the equivalent transfer functions of the simplified control links; and $G_i(s)$ is the transfer function of the PI regulator in the current loop. The expressions of the coefficients are as follows:

$$\begin{cases} G_1(s) = 1/\left[1 + sC_fK_dG_d(s) + s^2L_{f1}C_f\right] \\ G_2(s) = \left[1 + sC_fk_dG_d(s) + s^2L_{f1}C_f\right]/m_{de}(s) \\ m_{de}(s) = s(L_{f1} + L_{f2}) + s^2L_{f2}C_fk_dG_d(s) + s^3L_{f1}L_{f2}C_f \\ G_d(s) = e^{-1.5sT_s} \\ G_i(s) = k_p + k_i/s \\ H_{pll}(s) = k_{ppll} + k_{ipll}/s \\ T_{pll}(s) = H_{pll}(s)/\left[s - U_{gd}H_{pll}(s)\right] \end{cases} \quad (1)$$

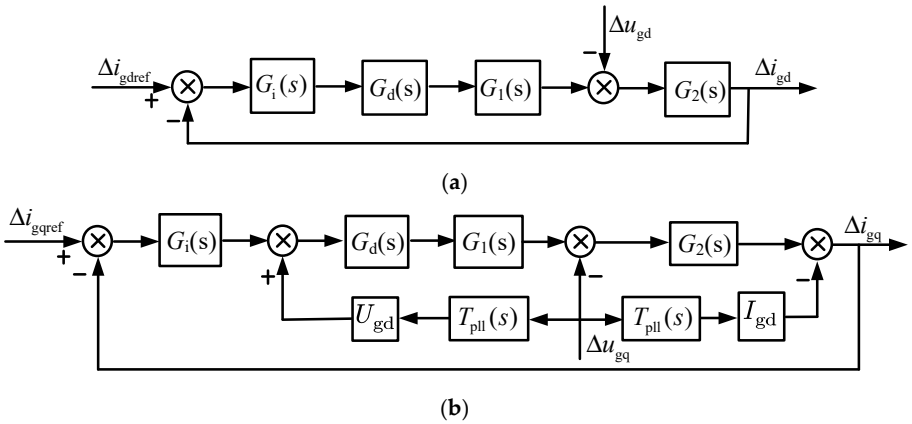

Figure 2. Closed-loop small-signal equivalent model of the DQ-axis of grid-connected inverter: (**a**) d-axis. (**b**) q-axis.

In the equation, k_{ppll} is the proportional coefficient of the PLL; k_{ipll} is the integral coefficient of the PLL; and T_s is the sampling time constant.

As shown in Figure 2, $\Delta\theta$ only affects the q-axis, which leads to poorer stability on the q-axis compared to the d-axis. The grid-connected inverter model established in this paper takes the influence of $\Delta\theta$ into account. To avoid repetitive analysis, the subsequent discussion focuses solely on the q-axis, which exhibits weaker stability. In this case, the output impedance expression of the grid-connected inverter is given by:

$$\begin{cases} T_A(s) = G_i(s)G_d(s)G_1(s)G_2(s) \\ Z(s) = \dfrac{1+T_A(s)}{G_2(s)+G_{pll}(s)T_A(s)\left(I_{gd}+\frac{U_{gd}}{G_i(s)}\right)} \end{cases} \tag{2}$$

In the equation, Z(s) denotes the output impedance of the inverter, and T_A(s) represents the forward channel gain.

3. Reshaped Impedance Criterion of Grid-Connected Inverters

3.1. Reshaped Impedance Criterion

The equivalent model of the grid-connected inverter is shown in Figure 3, where Z_g(s) denotes the grid impedance, U_g(s) the grid voltage, I_g(s) the grid-side current, and I_s(s) the inverter output current. According to Figure 3, the grid current can be expressed as:

$$\begin{cases} I_g(s) = H_{x1}(s)H_{x2}(s) \\ H_{x1}(s) = I_s(s) - U_g(s)/Z(s) \\ H_{x2}(s) = 1/[1 + Z_g(s)/Z(s)] \end{cases} \tag{3}$$

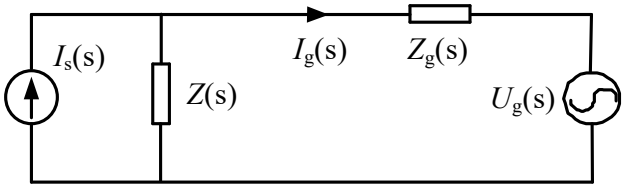

Figure 3. Equivalent model of grid-connected inverter.

According to Equation (3), the stability of the grid-connected system is jointly determined by H_{x1}(s) and H_{x2}(s). Among them, H_{x1}(s) involves only controller parameters, whose stability is ensured during the initial design stage, while H_{x2}(s) characterizes the dynamic interaction between the inverter output impedance and the grid impedance. Under weak grid conditions, variations in grid impedance may cause oscillatory instability in the control system. Therefore, H_{x2}(s) can serve as the stability criterion of the system under weak grid conditions. Based on the Nyquist stability criterion, when the control system is stable, the phase margin PM_1 at the crossover frequency of Z(s) and Z_g(s) is greater than zero, i.e., Equation (4) is greater than zero.

Reference [7] points out that the traditional stability criterion not only relies on H_{x2}(s) to evaluate the stability of the control system but also uses H_{x2}(s) to quantify the stability margin. However, the actual stability margin of the system is affected not only by H_{x2}(s) but also by H_{x1}(s). Therefore, the traditional stability margin evaluation method based solely on H_{x2}(s) introduces errors and cannot fully reflect the true stability of the system. The reference divides the inverter output impedance Z(s) into two parts, $Z_{t1}(s)$ and $Z_{t2}(s)$. In this case, the ratio $Z_{t1}(s)/\left[Z_{t2}(s) + Z_g(s)\right]$ is equivalent to the open-loop transfer function of the system. This newly defined impedance ratio can accurately reflect the stability margin of the current control loop and eliminates the steady-state errors inherent in traditional

methods. According to the conclusions on the reconstruction of the impedance criterion presented in the reference, the inverter output impedance model is as shown in Figure 4, where the expressions of the two impedance components in the d, q reference frame are given in Equation (5), and the corresponding phase margin calculation method is presented in Equation (6).

$$PM_1 = 180^\circ + \{\arg[Z(s)] - \arg[Z_g(s)]\} \tag{4}$$

$$\begin{cases} Z_{t1}(s) = \frac{T_A(s)}{G_{x2}(s)+G_{pll}(s)T_A(s)[I_{gd}+U_{gd}/G_i(s)]} \\ Z_{t2}(s) = \frac{1}{G_{x2}(s)+G_{pll}(s)T_A(s)[I_{gd}+U_{gd}/G_i(s)]} \end{cases} \tag{5}$$

$$PM_2 = 180^\circ - \{arg[Z_t(s)] - arg[Z_{t1}(s)]\} \tag{6}$$

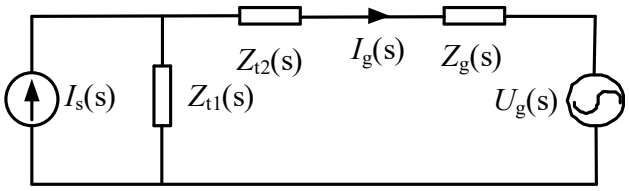

Figure 4. Reconstructs the equivalent model of the impedance criterion for grid-connected inverters.

In the equation, Z_t(s) is equal to the sum of Z_{t2}(s) and Z_g(s).

3.2. Comparison Between the Reshaped Impedance Criterion and the Traditional Criterion

As the reshaped impedance criterion proposed in Reference [7] fails to account for the influence of $\Delta\theta$ and the controller delay, this study, based on the previously established impedance model that considers both $\Delta\theta$ and controller delay, conducts a comparative analysis between the improved impedance criterion and the traditional impedance criterion to highlight the advantages of the improved method.

As shown in Figure 5, when L_g is 15 mH, the crossover frequency between Z_t(s) and Z_{t1}(s) is 105 Hz. At this frequency, the phase difference between Z_t(s) and Z_{t1}(s) ranges from 83.5° to 87.6°. According to Equation (10), the phase margin is calculated to be 8.9°. The cutoff frequency of TA(s) is also 105 Hz, where the phase is −171.1°, resulting in a phase margin of 8.9°. Therefore, under the reshaped impedance criterion, the control system is regarded as stable. Moreover, the phase margin obtained from the reshaped impedance criterion is equal to the actual phase margin of the open-loop transfer function.

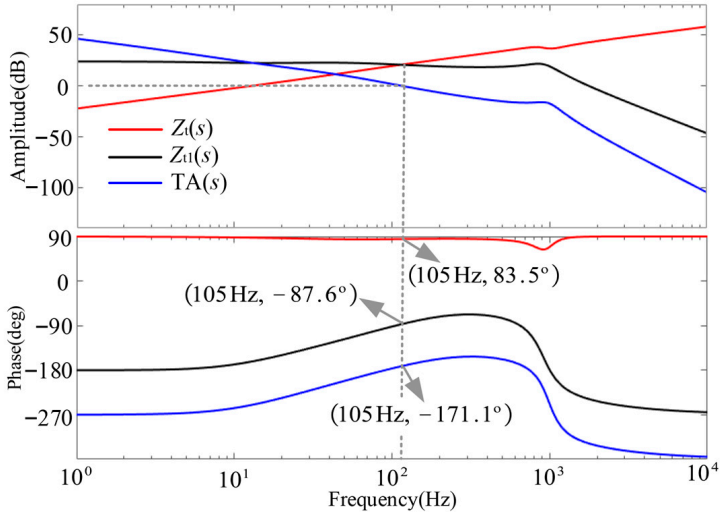

Figure 5. Impedance reshaping criterion when Lg is 15 mH.

As shown in Figure 6, when L_g is 15 mH and the traditional impedance criterion is applied, the crossover frequency between Z(s) and Z_g(s) is 102 Hz. At this frequency, the phase difference between Z(s) and Z_g(s) ranges from $-90.1°$ to $-90°$, and according to Equation (8), the phase margin is less than zero. In this case, the traditional impedance criterion concludes that the control system is unstable.

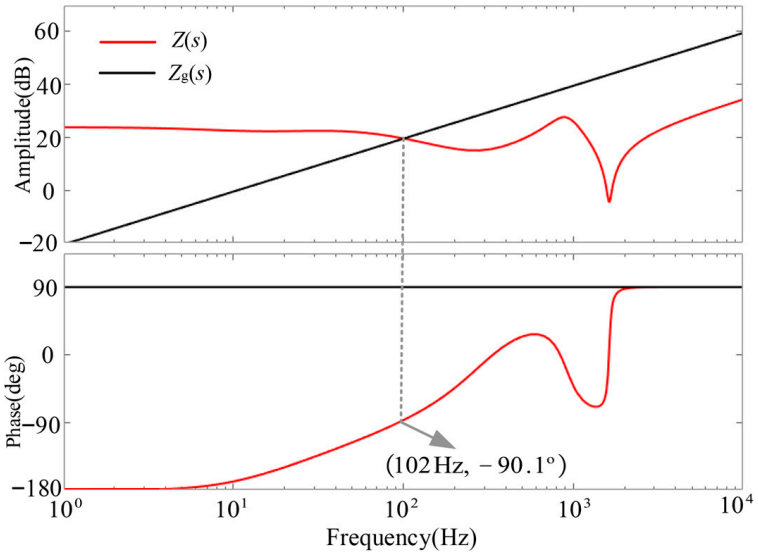

Figure 6. Traditional impedance criterion when Lg is 15 mH.

By comparing the results before and after applying the reshaped impedance criterion, it can be seen that the phase margin obtained through the reshaped criterion is consistent with the actual phase margin of the system's open-loop transfer function, accurately reflecting the system's stability margin. In contrast, the traditional impedance criterion provides results inconsistent with the actual system stability margin, leading to errors in stability assessment. The experimental validation of these results will be presented in Section 3.1.

As shown in Figure 6, the output impedance phase of Z(s) is less than $-90°$ in the low-frequency range, indicating that the control system is unstable within this frequency band. As the grid impedance increases, the crossover frequency gradually shifts toward the low-frequency region, which further leads to system instability.

3.3. q-Axis Control Compensation Strategy

To improve the phase of the inverter output impedance in the low-frequency range, Reference [12] introduces a disturbance feedback term into the q-axis to counteract the influence of PLL disturbance on the q-axis. As shown in Figure 7, after introducing disturbance compensation into the q-axis, its transfer function becomes identical to that of the d-axis in Figure 2a. In this case, the output impedance of the inverter is expressed as Equation (7), and the phase margin is given by Equation (8):

$$\begin{cases} Z_{t1}^{1}(s) = T_A(s)/G_{x2}(s) \\ Z_{t2}^{1}(s) = 1/G_{x2}(s) \end{cases} \tag{7}$$

$$PM_3 = 180° - \left\{ arg[Z_t^1(s)] - arg[Z_{t1}^1(s)] \right\} \tag{8}$$

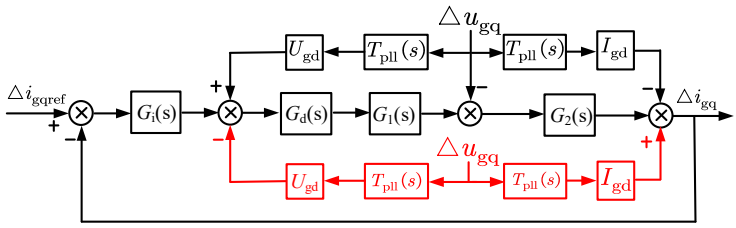

Figure 7. Disturbance feedback compensation introduced on the q-axis.

In the equation, $Z_t^1(s)$ is equal to the sum of $Z_{t1}^1(s)$ and Z_g(s).

When L_g is 15 mH and the q-axis introduces disturbance feedback compensation, the Bode diagram of the inverter output impedance and the grid impedance is as shown in Figure 8. At this time, the crossover frequency between $Z_t^1(s)$ and $Z_{t1}^1(s)$ is 121 Hz, and the phases of $Z_t^1(s)$ and $Z_{t1}^1(s)$ at the crossover frequency are 83.6° and −66.2°, respectively. According to Equation (8), the phase margin at this point is 30.2°. Compared with Figure 5, under the same grid impedance condition, after introducing disturbance compensation into the q-axis, the phase margin increases from 8.9° to 30.2°, thereby improving the robustness of the control system.

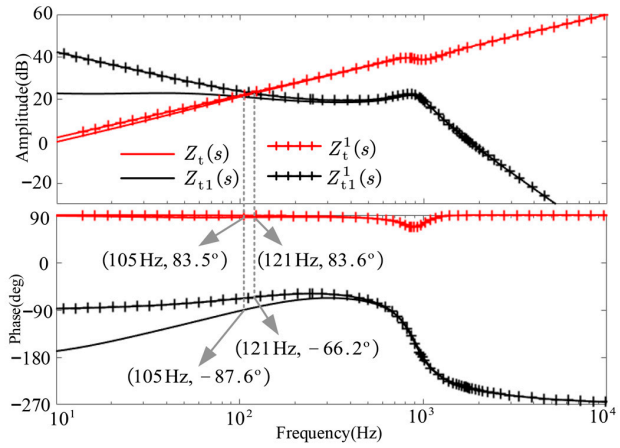

Figure 8. Bode plot of output impedance before and after compensation on the q-axis.

However, as the grid-side line inductance gradually decreases, instability occurs. As shown in Figure 9, when L_g is 3 mH, the crossover frequency between $Z_t^1(s)$ and $Z_{t1}^1(s)$ reaches up to 1280 Hz. At this frequency, the phases of $Z_t^1(s)$ and $Z_{t1}^1(s)$ are 44.9° and −207°, respectively, resulting in a phase margin less than zero, which indicates that the control system becomes unstable.

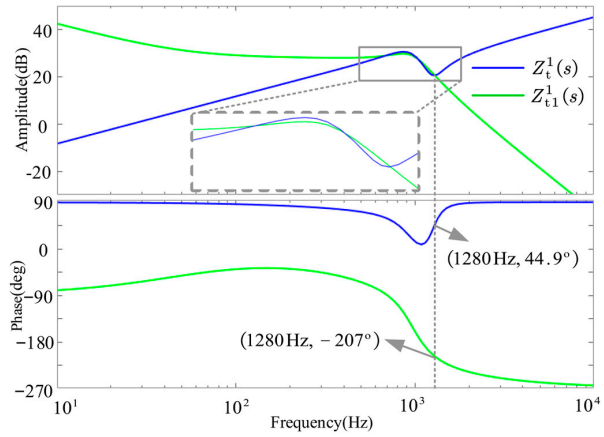

Figure 9. Bode plot of inverter output impedance when Lg is 3 mH.

3.4. Improved q-Axis Control Compensation Strategy

Reference [21] indicates that introducing derivative feedback into the control loop can enhance the phase of the system's open-loop transfer function. In Section 3.3, the phase of $Z_{t1}^{1}(s)$ in the high-frequency range is excessively low, resulting in a negative phase margin and consequent instability of the control system. This paper adopts the control concept of derivative feedback, however, considering the risk of harmonic amplification.

Associated with a derivative term, the integral transfer function H(s) proposed in Reference [22] is employed as an equivalent substitute. Its specific expression is given by Equation (9) as follows:

$$H(s) = \frac{k(\omega_c)^2 s}{s^2 + \omega_s s + (\omega_c)^2} \tag{9}$$

In the equation, ω_s denotes the cutoff angular frequency, ω_c represents the maximum gain angular frequency, and k is the proportional coefficient.

The Bode diagram of H(s) is shown in Figure 10. To ensure that H(s) maintains its derivative characteristics within the Nyquist frequency, ω_c should be set to πf_s, where f_s is the switching frequency. Within this frequency range, H(s) can effectively replace the derivative term. By adjusting ω_s, the gain at ω_c can be regulated, thereby effectively suppressing noise. After introducing the H(s)-based negative feedback, the control block diagram is as illustrated in Figure 11. At this point, the inverter output impedance and phase margin are given by Equations (10) and (11), respectively.

$$\begin{cases} Z_{t1}^{2}(s) = T_A(s)/[G_{x2}(s) + kH(s)T_A(s)/G_i(s)] \\ Z_{t2}^{2}(s) = 1/[G_{x2}(s) + kH(s)T_A(s)/G_i(s)] \end{cases} \tag{10}$$

$$PM_3 = 180^\circ - \left\{ arg[Z_t^2(s)] - arg[Z_{t1}^2(s)] \right\} \tag{11}$$

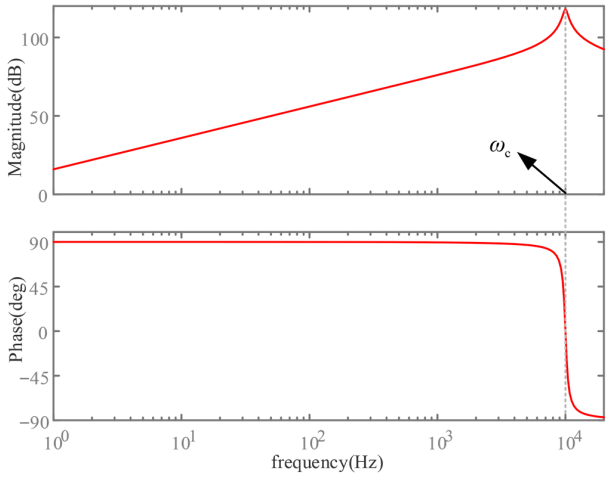

Figure 10. Bode plot of H(s) with k = 1.

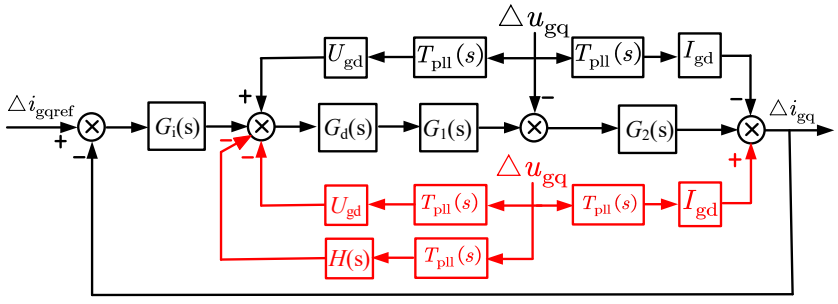

Figure 11. Q-axis improved control compensation strategy.

In the equation, $Z_t^2(s)$ is equal to the sum of $Z_{t1}^2(s)$ and Z_g(s).

Under the condition of L_g = 3 mH, Figure 12 compares the effects of different k values on the output impedance. When k = 0.3, the crossover frequency between $Z_t^2(s)$ and $Z_{t1}^2(s)$ is 1060 Hz, and the phases of $Z_t^2(s)$ and $Z_{t1}^2(s)$ at the crossover frequency are 41° and −191°, respectively. According to Equation (11), the phase margin is less than zero. When k = 0.5, the crossover frequency is 630 Hz, and the corresponding phases are 49.4° and −111°, giving a phase margin of 19.6°. When k = 0.8, the crossover frequency is 725 Hz, and the corresponding phases are 42.4° and −136°, resulting in a phase margin of 1.6°. It can be observed that as k increases, the crossover frequency of the impedance decreases first and then increases, while the phase margin increases first and then decreases. Therefore, a value of k = 0.5 is chosen as a compromise.

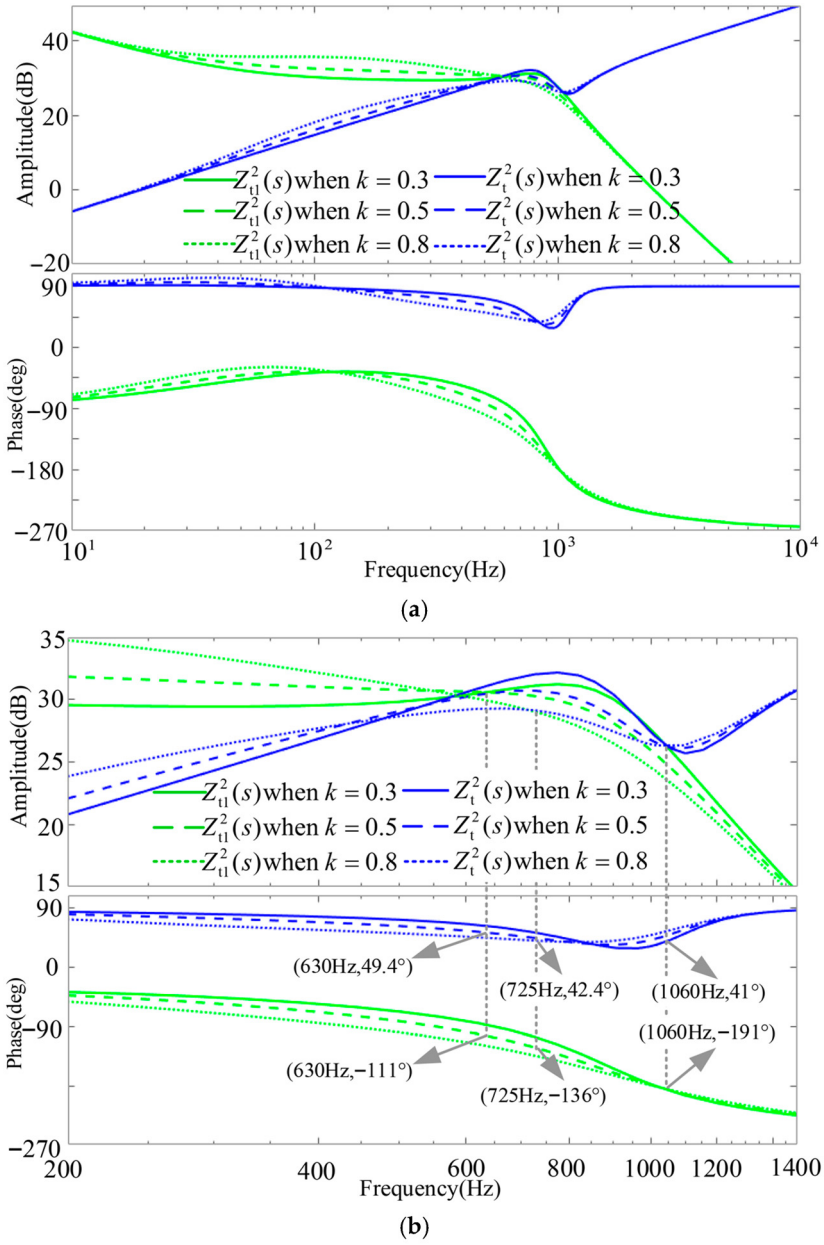

Figure 12. Bode plot of output impedance at different k values: (**a**) Overall Schematic Diagram. (**b**) Locally Enlarged View from 200 Hz to 1400 Hz.

When k = 0.5 and L_g = 3 mH, adopting the improved q-axis control compensation strategy can stabilize the control system and expand the adaptability range of the system to

grid impedance. As shown in Figure 13, when the grid impedance is further reduced to 0, the crossover frequency between $Z_t^2(s)$ and $Z_{t1}^2(s)$ is 701 Hz, and the phases of $Z_t^2(s)$ and $Z_{t1}^2(s)$ at the crossover frequency are 36.4° and −132°, respectively. At this point, the phase margin is 11.6°, and the control system remains stable. It can be seen that by applying the improved q-axis control compensation strategy, the inverter can operate stably with grid impedance ranging from 0 to 15 mH, significantly enhancing the adaptability of the control system to grid impedance variations.

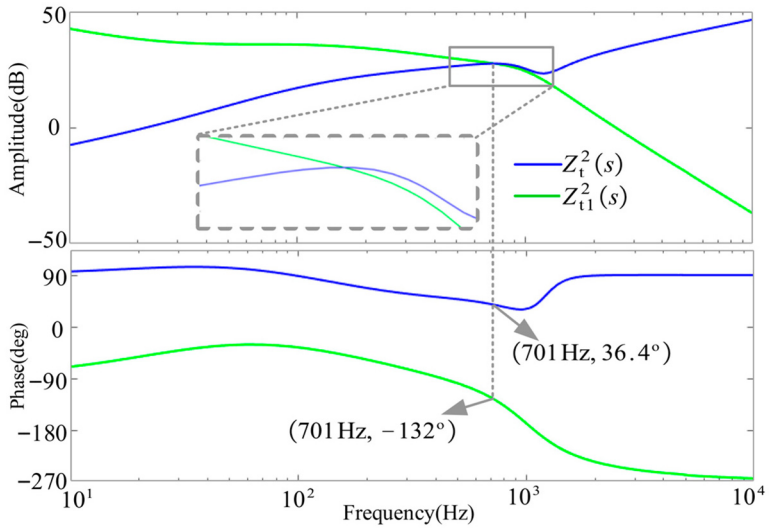

Figure 13. Bode plot of output impedance with improved control compensation when L_g is 0.

4. Experimental Validation

To verify the correctness of the above theoretical analysis, a three-phase grid-connected inverter experimental platform with a rated capacity of 10 kVA was built, as shown in Figure 14. The experimental platform consists of a DC power supply, an oscilloscope, a grid simulator, and a 10 kVA inverter. The inverter includes the main control with a sampling board, a power board, and an LCL filter board. The waveforms of the grid-connected voltage and current are measured using the oscilloscope. The parameters of the experimental platform are listed in Table 1.

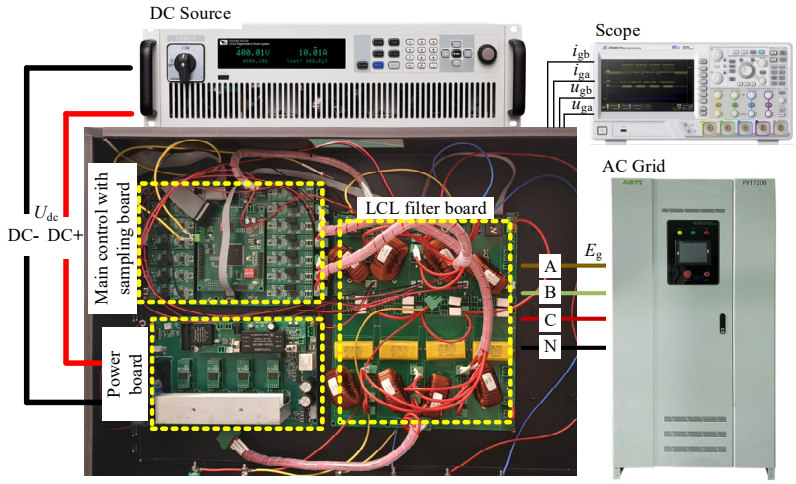

Figure 14. 10 kVA experimental platform.

Table 1. Key system parameters.

Parameter	Symbol	Value
DC Voltage	U_{dc}	700 V
Grid Voltage	E_g	311 V
Rated Capacity	S_n	10 kVA
Filter Inductance1	L_{f1}	3 mH
Filter Inductor2	L_{f2}	0.8 mH
Filter Capacitor	C_f	15 uF
Switching Frequency	f_s	10 kHz
Active Damping Coefficient	K_d	13
Proportional Coefficient of the Current Loop	k_p	2
Integral Coefficient of the Current Loop	k_i	350
Proportional Coefficient of PLL	k_{ppll}	0.8
Integral Coefficient of PLL	k_{ipll}	32
Proportional Coefficient	k	0.5
Cutoff Angular Frequency	ω_s	5000 rad/s
Maximum Gain Angular Frequency	ω_c	$10^4\pi$ rad/s

4.1. Experimental Comparison Before and After Impedance Criterion Reshaping

When grid inductance L_g = 15 mH operates without q-axis control compensation, with reference currents set at i_{gdref} = 21.4 A and i_{gqref} = 0 A, comparative stability analysis in Section 3.2 shows the conventional impedance criterion predicts instability while the proposed reshaped criterion confirms stability. Experimental results in Figure 15 demonstrate stable system operation, with grid-connected current THD measuring 2.85% in Figure 16a, complying with grid standards. This validates the reshaped criterion's accuracy and reveals the conventional criterion's stability misjudgment.

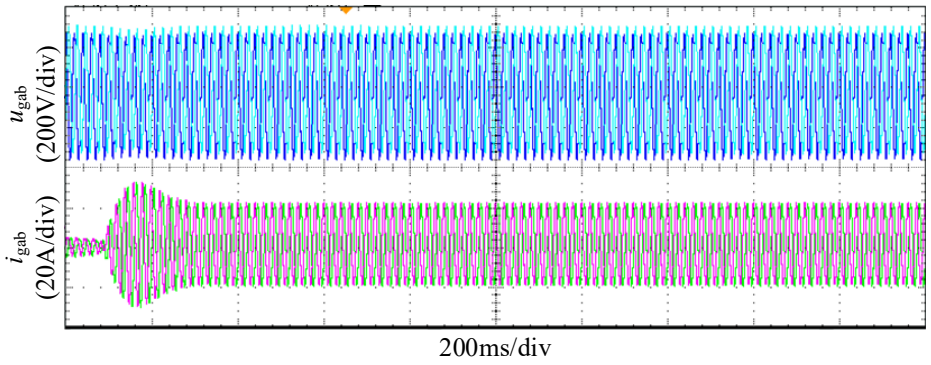

Figure 15. Grid-connected voltage and current without control compensation when L_g is 15 mH.

4.2. Experimental Analysis of q-Axis Control Compensation Introduction

Following the implementation of q-axis control compensation, experiments were conducted under two grid inductance conditions: L_g = 15 mH and L_g = 3 mH, with reference currents set at i_{gdref} = 21.4 A and i_{gqref} = 0 A. The corresponding grid voltage and current waveforms are presented in Figures 17 and 18, respectively. Analysis of Figure 17 demonstrates that the control system maintains stable operation with L_g = 15 mH under control compensation, where the grid-connected current total harmonic distortion (THD) measures 1.29% as shown in the spectrum in Figure 16b, complying with grid code requirements. However, when the grid inductance decreases to 3 mH, the system exhibits evident oscillatory instability, as shown in Figure 18. These experimental results indicate that after implementing q-axis control compensation, the control system becomes susceptible to instability risks under reduced grid impedance conditions.

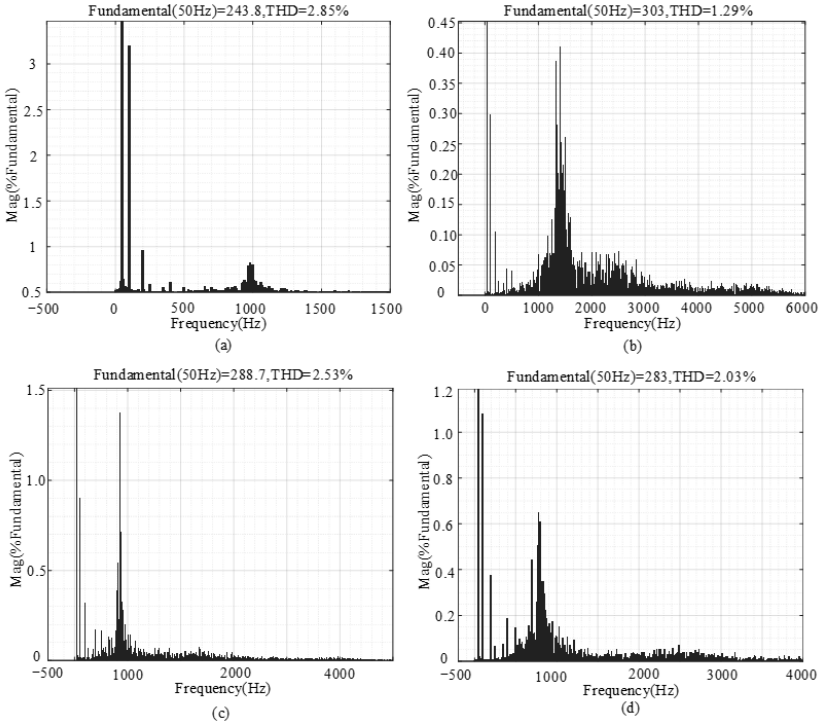

Figure 16. Grid-connected current THD: (**a**) L_g = 15 mH without control compensation. (**b**) L_g = 15 mH with conventional control compensation. (**c**) L_g = 3 mH with improved control compensation. (**d**) L_g = 0 mH with improved control compensation.

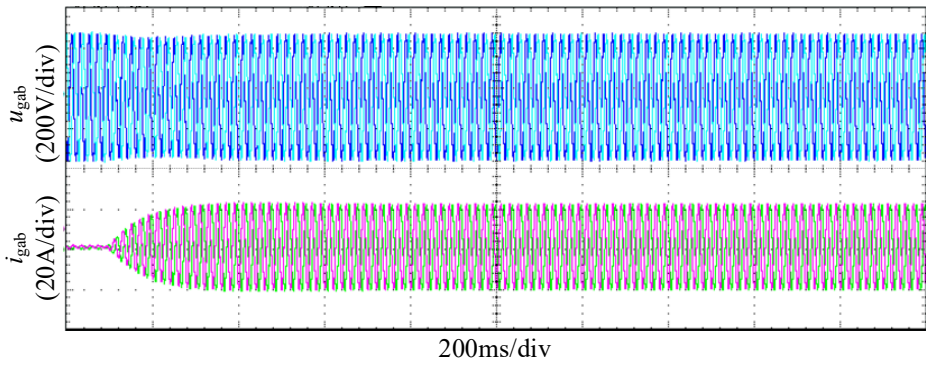

Figure 17. Grid-connected voltage and current with control compensation when L_g is 15 mH.

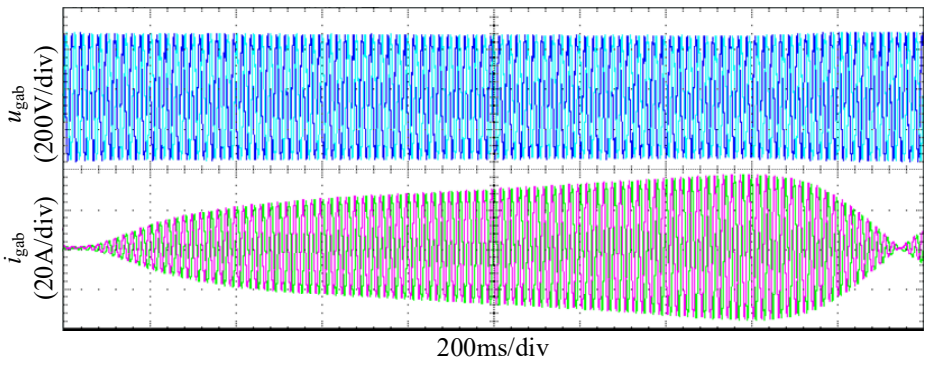

Figure 18. Grid-connected voltage and current with control compensation when L_g is 3 mH.

4.3. Experimental Analysis of the Improved q-Axis Control Compensation

Under the condition of grid inductance L_g = 3 mH with the improved q-axis control compensation implemented, experimental validation was conducted for three parameter

configurations of compensation coefficient k: 0.3, 0.5, and 0.8. The experimental results are shown in Figure 19. The findings demonstrate that: when k = 0.3, the control system becomes unstable; when k = 0.5, the system maintains stable operation with a grid-connected current total harmonic distortion (THD) of 2.53%, whose spectral distribution is shown in Figure 16c, meeting the grid power quality requirements; when k increases to 0.8, the control system again exhibits instability due to insufficient phase margin. The stability performance under different k values is fully consistent with the theoretical analysis presented in Section 3.4.

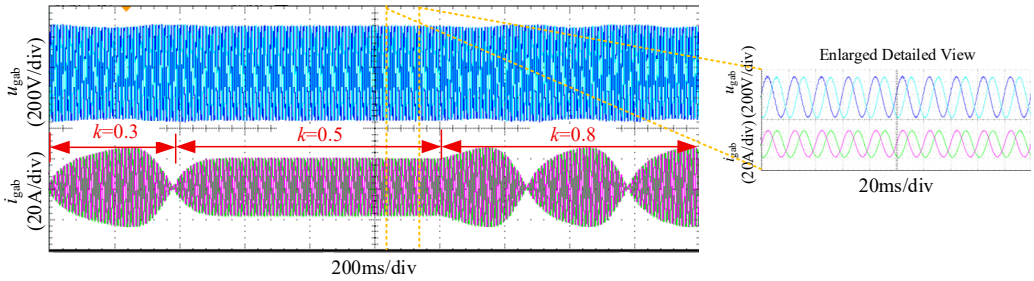

Figure 19. Influence of k on Stability.

Under the improved q-axis control compensation parameter (k = 0.5), experiments were conducted under the condition of grid inductance L_g = 0 mH, with reference currents set to i_{gdref} = 21.4 A and i_{gqref} = 0 A. The experimental results are shown in Figure 20. Observations demonstrate that with the improved control compensation algorithm, the control system maintains stable operation under this condition. The grid-connected current total harmonic distortion (THD) was measured at 2.03%, with its spectral distribution shown in Figure 16d, meeting the grid power quality requirements. These results effectively verify the significant role of the proposed method in enhancing the system's adaptability to grid impedance variations.

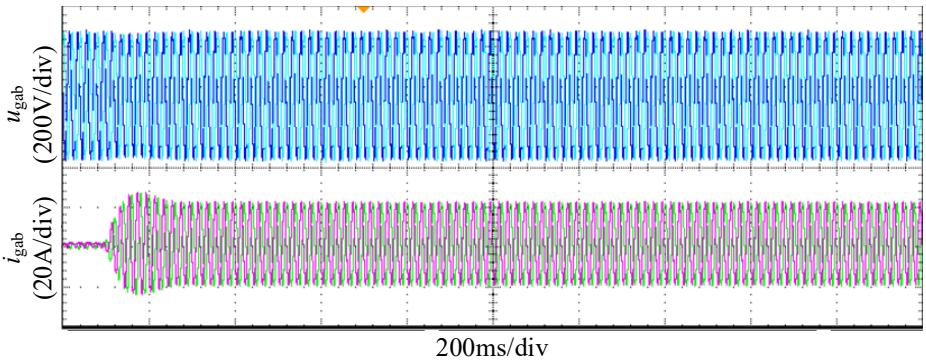

Figure 20. Grid-connected voltage and current with improved control compensation when L_g is 0.

As evidenced by the preceding analysis and experimental results, when the grid impedance L_g varies over a wide range, the admissible ranges of L_g for both conventional and improved compensation control methods are summarized in Table 2. The conventional compensation control can accommodate L_g values from 3 mH to 15 mH, whereas the improved compensation control extends this range to 0–15 mH. This demonstrates that the improved compensation control offers a broader grid impedance adaptability, making it more suitable for practical engineering applications under modern weak grid conditions where grid impedance frequently fluctuates.

Table 2. Stable operating range for L_g.

Control Method	Stable Operating Range for L_g
Traditional compensation control	3–15 mH
Improved compensation control	0–15 mH

5. Conclusions

This paper starts by addressing the issue of errors introduced by traditional impedance criteria in characterizing stability margins and systematically analyzes the causes of inaccuracies in the traditional criterion. Based on the reshaped impedance criterion method, the stability and stability margins of the control system are investigated in depth. The study shows that the PLL generates small-signal disturbances under the influence of grid impedance, which can lead to inverter instability under high-grid-impedance conditions. Although traditional q-axis compensation control can improve the adaptability of the inverter under high grid impedance, instability issues still exist under low-grid-impedance conditions. Based on this, this paper proposes an improved q-axis compensation control strategy and further analyzes the output impedance characteristics of the improved control in conjunction with the reshaped impedance criterion. The main conclusions are as follows:

(1) The reshaped impedance criterion method can accurately characterize the actual phase margin of the control system, effectively resolving the phase error inherent in traditional impedance criteria, and provides a more precise tool for stability analysis in practical applications. This method significantly enhances the accuracy of system stability assessments, especially in areas where grid impedance varies significantly.

(2) The proposed improved q-axis compensation control not only enhances the adaptability of the inverter under high-line-impedance conditions but also addresses the instability problem under low-line-impedance conditions, thereby significantly expanding the adaptability range of the grid impedance. In addition, the impedance model established based on the reshaped impedance criterion can accurately reflect the actual phase margin of the system, completely avoiding the characterization errors of traditional methods.

(3) The method proposed in this study has great potential for practical engineering applications. By improving the inverter control strategy, it can effectively enhance stability under various grid conditions and provide strong support for the optimization of renewable energy grid integration systems. It also offers technical guarantees for the construction of smart grids and future power systems.

Author Contributions: Conceptualization, H.M. and X.Y.; Methodology, H.M. and X.Y.; Software, H.M.; Validation, H.M.; Formal analysis, H.M. and X.Y.; Investigation, H.M. and X.Y.; Resources, X.Y.; Data curation, H.M.; Writing—original draft, H.M.; Writing—review & editing, H.M. and X.Y.; Visualization, H.M. and X.Y.; Supervision, X.Y.; Project administration, H.M. and X.Y.; Funding acquisition, X.Y. All authors have read and agreed to the published version of the manuscript.

Funding: This research received no external funding.

Data Availability Statement: The original contributions presented in this study are included in the article. Further inquiries can be directed to the corresponding author.

Conflicts of Interest: The authors declare no conflict of interest.

References

1. Wilk-Jakubowski, J.L.; Pawlik, L.; Wilk-Jakubowski, G.; Harabin, R. State-of-the-Art in the Use of Renewable Energy Sources on the Example of Wind, Wave Energy, Tidal Energy, and Energy Harvesting: A Review from 2015 to 2024. *Energies* **2025**, *18*, 1356. [CrossRef]
2. Azam, M.A.; Khan, M.R.; Saeed, A. A Review of Sustainable Energy Sources Using Machine Learning. *Energies* **2023**, *16*, 6236.
3. Mimouni, A.; Laribi, S.; Bizhani, H.; Iwanski, G. Switch Fault Diagnosis of Grid-Connected Inverter Using Symmetrical Components. *IEEE J. Emerg. Sel. Top. Power Electron.* **2024**, *12*, 5258–5272. [CrossRef]
4. Pang, Y.; Li, Y.; Zhang, J.; Yang, H.; Ji, Y.; Zhang, X.; Zhu, Y.; Li, G.; Xiang, Z.; Gong, C.; et al. A Multiple Energy Conversion Channels Fusion Grid-Connected Inverter for Large-Scale PV Active Power Injection Preventing Power Loss Caused by Insufficient MPP PV Voltage. *IEEE Trans. Power Electron.* **2025**, *40*, 13415–13433. [CrossRef]
5. Malkhandi, A.; Senroy, N.; Mishra, S. A Dynamic Model of Impedance for Online Thevenin's Equivalent Estimation. *IEEE Trans. Circuits Syst. II Express Briefs* **2022**, *69*, 194–198. [CrossRef]
6. Jin, Z.; Wang, X. A DQ-Frame Asymmetrical Virtual Impedance Control for Enhancing Transient Stability of Grid-Forming Inverters. *IEEE Trans. Power Electron.* **2022**, *37*, 4535–4544. [CrossRef]
7. Wang, Y.; Wang, X.; Blaabjerg, F.; Chen, Z. Harmonic Instability Assessment Using State-Space Modeling and Participation Analysis in Inverter-Fed Power Systems. *IEEE Trans. Ind. Electron.* **2017**, *64*, 806–816. [CrossRef]
8. Cai, Y.; He, Y.; Zhang, H.; Zhou, H.; Liu, J. Research on Harmonic State-Space Modeling and Calculation Analysis of Low-Switching-Frequency Grid-Connected Inverter Considering the Impact of Digitization. *IEEE Trans. Power Electron.* **2023**, *38*, 1003–1021. [CrossRef]
9. Li, Z.; Li, H.; Sun, S. Virtual Model Predictive Control for Inverters to Achieve Flexible Output Impedance Shaping in Harmonic Interactions With Weak Grids. *IEEE Trans. Power Electron.* **2024**, *39*, 10754–10767. [CrossRef]
10. Qian, Q.; Xie, S.; Xu, J.; Xu, K.; Bian, S.; Zhong, N. Output Impedance Modeling of Single-Phase Grid-Tied Inverters With Capturing the Frequency-Coupling Effect of PLL. *IEEE Trans. Power Electron.* **2020**, *35*, 5479–5495. [CrossRef]
11. Gao, J.Y.; Zhao, J.B.; Chen, X.B.; Qu, K. Reshaped Impedance-Based Stability Criterion Under Weak Grid Conditions. *Power Syst. Technol.* **2017**, *41*, 2762–2768. (In Chinese)
12. Zhu, D.H.; Zhou, S.Y.; Zou, X.D.; Kang, Y. Improved Design of PLL Controller for LCL-Type Grid-Connected Converter in Weak Grid. *IEEE Trans. Power Electron.* **2020**, *35*, 4715–4727. [CrossRef]
13. Gao, J.Y.; Xiao, F.; Jiang, F.; Guo, Q.; Lu, B.H. Grid-Connected Inverter Impedance Phase Reshaping Control With Novel PLL Structure in Weak Grid. *Proc. CSEE* **2020**, *40*, 6682–6694. (In Chinese)
14. Karimi-Ghartemani, M.; Karimi, H.; Khajehoddin, S.A.; Hoseinizadeh, S.M. Efficient Modeling and Systematic Design of Enhanced Phase-Locked Loop Structures. *IEEE Trans. Power Electron.* **2022**, *37*, 9061–9072. [CrossRef]
15. Yang, D.; Ruan, X.; Wu, H. A Virtual Impedance Method to Improve the Performance of LCL-Type Grid-Connected Inverters Under Weak Grid Conditions. *Proc. CSEE* **2014**, *34*, 2327–2335. (In Chinese)
16. Lin, X.; Liang, Z.; Zheng, Y.; Lin, Y.; Kang, Y. A Current Limiting Strategy with Parallel Virtual Impedance for Three-Phase Three-Leg Inverter Under Asymmetrical Short-Circuit Fault to Improve the Controllable Capability of Fault Currents. *IEEE Trans. Power Electron.* **2019**, *34*, 8138–8149. [CrossRef]
17. Zhu, D.H.; Zhou, S.Y.; Zou, X.D.; Kang, Y.; Zou, K. Small-Signal Disturbance Compensation Control for LCL-Type Grid-Connected Converter in Weak Grid. *IEEE Trans. Ind. Appl.* **2020**, *56*, 2852–2861. [CrossRef]
18. Wen, B.; Boroyevich, D.; Burgos, R.; Mattavelli, P.; Shen, Z. Analysis of D-Q Small-Signal Impedance of Grid-Tied Inverters. *IEEE Trans. Power Electron.* **2016**, *31*, 675–687. [CrossRef]
19. Tu, C.M.; Gao, J.Y.; Xiao, F.; Guo, Q.; Jiang, F. Stability Analysis of the Grid-Connected Inverter Considering the Asymmetric Positive Feedback Loops Introduced by the PLL in Weak Grids. *IEEE Trans. Ind. Electron.* **2022**, *69*, 5793–5802. [CrossRef]
20. Zhou, S.; Zou, X.; Zhu, D.; Tong, L.; Zhao, Y.; Kang, Y.; Yuan, X. An Improved Design of Current Controller for LCL-Type Grid-Connected Converter to Reduce Negative Effect of PLL in Weak Grid. *IEEE J. Emerg. Sel. Top. Power Electron.* **2018**, *6*, 648–663. [CrossRef]
21. Yu, H.; Su, J.; Zheng, L.; Zhang, T.; Zhang, D.; Shi, Y. Mechanism Analysis and Suppression Method of Sub-Synchronous Resonance for Energy Storage Inverter Connected to Grid. *Autom. Electr. Power Syst.* **2020**, *44*, 99–108. (In Chinese)
22. Xin, Z.; Loh, P.C.; Wang, X.; Blaabjerg, F.; Tang, Y. Highly Accurate Derivatives for LCL-Filtered Grid Converter with Capacitor Voltage Active Damping. *IEEE Trans. Power Electron.* **2016**, *31*, 3612–3625. [CrossRef]

Disclaimer/Publisher's Note: The statements, opinions and data contained in all publications are solely those of the individual author(s) and contributor(s) and not of MDPI and/or the editor(s). MDPI and/or the editor(s) disclaim responsibility for any injury to people or property resulting from any ideas, methods, instructions or products referred to in the content.